Cement and Concrete Research 180 (2024) 107502

Contents lists available at ScienceDirect

Cement and Concrete Research

journal homepage: www.elsevier.com/locate/cemconres

A kinetic Monte Carlo study of the C_3S dissolution mechanism

Pablo Martin [a,c,*], Juan J. Gaitero [b], Xabier M. Aretxabaleta [a], Mohammad Javad Abdolhosseini Qomi [c], Hegoi Manzano [a]

[a] Department of Physics, University of the Basque Country UPV/EHU, Barrio Sarriena s/n, 48940, Leioa, Bizkaia, Spain
[b] TECNALIA, Basque Research and Technology Alliance (BRTA) Parque Tecnológico de Bizkaia, Astondo Bidea, Edificio 700, 48160, Derio, Spain
[c] Department of Civil and Environmental Engineering, University of California, Irvine, CA 92697, United States

ARTICLE INFO

Keywords:
Kinetic Monte Carlo
Dissolution mechanism
C_3S
Alite
Dislocations
Dissolution rate
Activation energy

ABSTRACT

Understanding the mechanism that controls cement hydration and its stages is a long-standing challenge. Over a decade ago, the mineral dissolution theory was adopted from geochemistry to explain the hydration rate evolution of alite. The theory is not fully accepted by the community and deserves further investigation. In this work, we apply Kinetic Monte Carlo (KMC) simulations with the mineral dissolution theory as a conceptual framework to investigate and discuss alite dissolution. We build a Kossel crystal model system and parameterize the dissolution activation energies and frequencies based on experimental data. The resulting KMC model is capable of reproducing the dissolution rate and activation energies as a function of the dissolution free energy. The simulations indicate that mineral dissolution theory easily explains the induction and acceleration stages due to a continuous increase of the reactive area as the etch pits open. However, the deceleration stage is hardly reconcilable with the mechanism suggested in the literature, *i.e.* dislocation coalescence. Still, within the mineral dissolution theory umbrella, we propose and discuss an alternative mechanism based on dislocation exhaustion.

1. Introduction

Cement hydration is the process by which the cement powder, in contact with water, becomes a fluid paste and hardens into a solid material. Most properties of the final material depend on the hydration process, and there is a huge empirical knowledge about how to control the rate and the extent of the different hydration stages. Cement hydration is usually quantified by looking at calorimetry curves [1], which show the heat released during the dissolution as a function of time. The evolution of the heat release is proportional to the dissolution rate and indicates several well-differentiated stages in cement hydration, see Fig. 1a. After very fast hydration in the first few minutes, there is an induction period of about an hour in which the hydration rate is very low. Then, there is an acceleration stage until a maximum rate is reached at around 10 h. Beyond the maximum, the dissolution rate decelerates until it becomes almost negligible after some days.

A considerable number of theories have been proposed to explain the different stages, as reviewed in [1,3–7]. The most recent studies can be divided into two main groups depending on the rate controlling mechanism: C-S-H nucleation and growth controlled hydration, and alite dissolution controlled hydration. The C-S-H nucleation and growth interpretation states that the changes in the pore solution concentration due to the formation of hydration products, mainly C-S-H and portlandite, modify the free energy difference between the solid and the solution ΔG, altering the dissolution rate. The acceleration would correspond to an increasing undersaturation of the pore solution due to the precipitation of hydration products. Then, the transition from acceleration to deceleration has been attributed to a slowdown in the C-S-H nucleation and growth. The slowdown has been explained in the literature associated in general to lack of space: starting from an Avrami-like nucleation and growth [8], including the Boundary Nucleation and Growth [9], C-S-H densification [10], C-S-H anisotropic growth [11], needle-like C-S-H growth [12], or the existence of a limited reaction zone for the C-S-H formation [13].

The dissolution theory, which we explore in this paper, has been borrowed from the field of geochemistry [14,15]. Summarizing, the dissolution of a mineral surface can be classified into three mechanisms related to the surface topology and the free energy difference between the solid and the solution ΔG:

$$\Delta G = RT \ln \frac{\Pi}{K_s} = RT \ln \beta \tag{1}$$

where R is the ideal gas constant, T is the temperature, Π is the activity coefficient of the dissolved species and K_s their solubility product. The fraction Π / K_s is known as the saturation index β. Depending on the

* Corresponding author at: Department of Physics, University of the Basque Country UPV/EHU, Barrio Sarriena s/n, 48940, Leioa, Bizkaia, Spain.
E-mail addresses: pablo.martin@ehu.eus (P. Martin), hegoi.manzano@ehu.eus (H. Manzano).

https://doi.org/10.1016/j.cemconres.2024.107502
Received 1 August 2023; Received in revised form 17 January 2024; Accepted 31 March 2024
Available online 9 April 2024

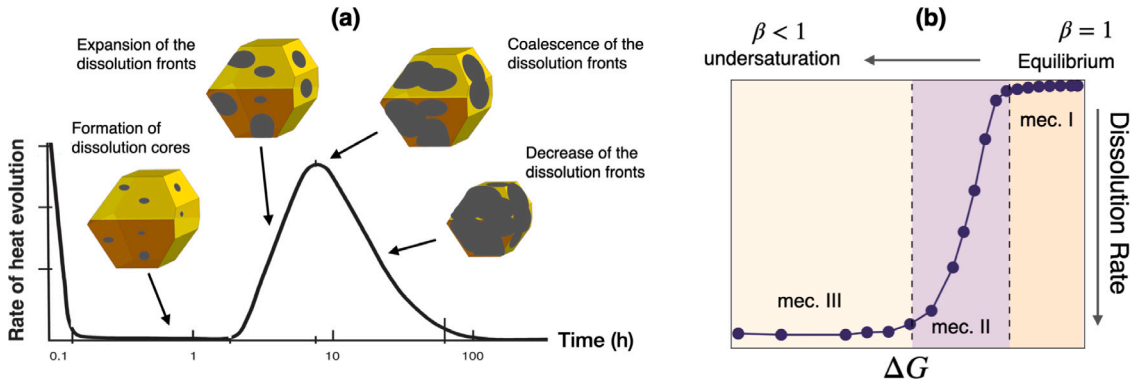

Fig. 1. (a) A typical calorimetry curve for the cement hydration. According to the dissolution theory, alite dissolution is responsible for the different stages. Induction period: initial low alite dissolution as its dislocations start to open. Acceleration period: Alite dissolution increase as dislocations keep opening. Deceleration period: dislocations start to coalesce, and alite particles shrink. Adapted from [2] (b) Typical sigmoid function of the dissolution rate with Gibbs free energy in the dissolution of mineral. Depending on the saturation index β, three mechanisms are observed. Mechanism I: At close to equilibrium conditions, the dissolution rate is low due to the low dissolution of initial irregularities on the mineral surface. Mechanism II: In the so called critical ΔG, the dissolution rate sharply increases due to the dislocation opening. Mechanism III: Some minerals far from equilibrium conditions present spontaneous pit openings, where any surface atom can become a dissolution core.

saturation index, different dissolution mechanisms can be observed in the mineral surface (see Fig. 1b). Close to equilibrium in mechanism I, the dissolution takes place only by step retreat of the surface roughness leading to a low dissolution rate. At intermediate undersaturation, in mechanism II, the existing dislocations open into dissolving etch pits. Finally, for some minerals far from equilibrium, in mechanism III, etch pits open at any point in the surface, leading to a high dissolution rate [16,17]. In the case of Alite dissolution, the three mechanisms are observed [2,16,18].

Several works have explored in detail the implications of mineral dissolution theory on C_3S, and alite hydration [2,16,18–20]. The initial deceleration towards the dormant period has been attributed to a transformation of the C_3S surface due to the initial reactions when the material is put in contact with water, the release of the first ions to solution, and the consequent decrease of the undersaturation towards values closer to equilibrium. The acceleration would correspond to a continuous increase in the reactive area of C_3S as dislocations open into etch pits [2]. The undersaturation is moderate, and C_3S dissolves in the mechanism II regime, where the dissolution of flat surfaces is negligible and etch pit growth is dominating dissolution. If it is considered that the global dissolution rate R_g is equal to the local rate at C_3S surfaces R_l times the reactive area S_r

$$R_g = S_r \cdot R_l \tag{2}$$

S_r increases continuously as the etch pits grow, and consequently, R_g increases. It is interesting to note that only the reactive area S_r should increase according to Eq. (2), and the proposed mechanism would be valid as far as grains do not shrink noticeably during the first hours. Following the same logic, the deceleration would result from a decrease in the reactive area. It has been suggested that the overall shrinkage of the C_3S grains and the coalescence of the etch pits as they grow could be two possible mechanisms to decrease S_r.

The boundary between the nucleation and growth and the dissolution theories is blurred since both rely up to a great extent on the over/under saturation of the pore solution with respect to the C-S-H and alite, respectively. Very likely, both mechanism coexists, yet it is still interesting to understand their relative contribution. In this work, we focused on the dissolution theory of alite [2], ignoring the precipitation of hydration products. In doing so, we performed Kinetic Monte Carlo simulations on an alite model system. First, we determine the parameters necessary to reproduce experimental data of alite dissolution and discuss their implication. Second, we test the role of dislocations, their coalescence, and their length. We show how dislocation opening can induce an acceleration in the hydration rate until a maximum value. However, the coalescence of adjacent etch pits does not decrease the rate as the reactive area remains constant. As an alternative, we suggest that the deceleration originates from the exhaustion of the existing dislocations.

2. Computational methods and models

2.1. Kinetic Monte Carlo model

In this work, we use Kinetic Monte Carlo (KMC) simulations to investigate the dissolution mechanism of C_3S at the microscale. KMC simulations describe the evolution of a system based on the probabilities of the individual events that may take place. In dissolution processes, these events can be explicit chemical reactions or a more general 'detachment' of particles from the solid. The rate of each dissolution event is calculated as follows:

$$r_d = f_d \cdot \exp\left(-\frac{E_d(n)}{k_b \cdot T}\right) \tag{3}$$

where f_d is the fundamental frequency of the dissolution event and $E_d(n)$ is the reaction activation energy, usually written as a function of the coordination (or the number of bonds) of the dissolving site n, and k_b the Boltzmann constant. At far from equilibrium conditions, Eq. (3) is enough to reproduce the dissolution rate if f_d and $E_d(n)$ are known. However, as we approach the equilibrium state between the dissolving solid and the species in the pore solution, the dissolution becomes slower, following a sigmoidal curve (see Fig. 1) [17]. To take into account the evolution of the dissolution rate with the undersaturation, we have developed a reversible KMC scheme that includes the microscopic reversibility of the chemical reactions adding a 'precipitation' event [17]:

$$r_p = f_p \cdot \exp\left(-\frac{E_p(n)^*}{k_b \cdot T}\right) \tag{4}$$

where f_p is the fundamental frequency of the precipitation event and $E_p(n)^*$ the effective precipitation activation energy. $E_p(n)^*$ depends on the equilibrium with the pore solution through the effective dissolution free energy ΔG^*:

$$E_p(n)^* = E_p(n) - \Delta G^* \tag{5}$$

The ΔG^* is large at far from equilibrium conditions, and the precipitation term becomes negligible. Close to equilibrium ΔG^* is lower, the precipitation term becomes important. The interplay between precipitation and dissolution allows the reproduction of the typical sigmoidal curve of the dissolution rate with ΔG. Finally, ΔG^* reaches a value at which the dissolution and precipitation rates are equal $E_d(n) = E_p(n) - \Delta G^*$, and the system is at equilibrium. It must be clear that

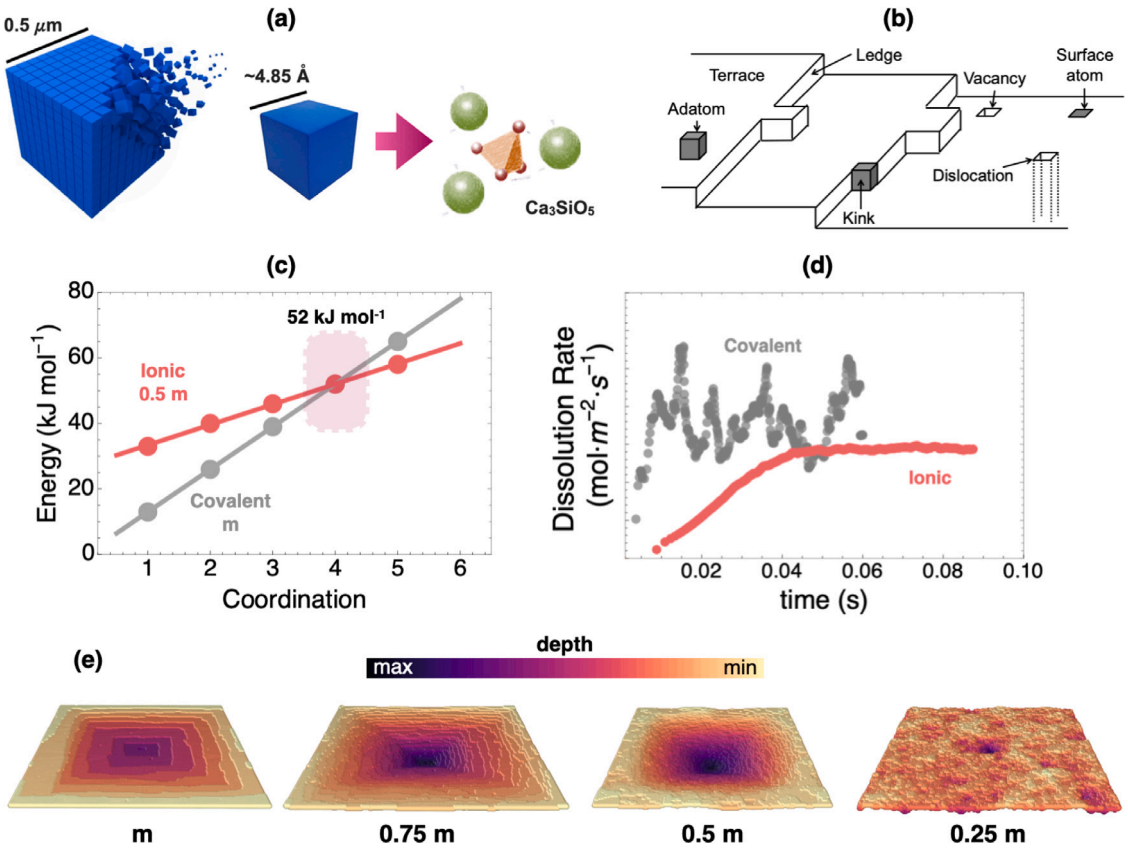

Fig. 2. (a) Coarse grain scheme of the C3S crystal (b) Representation of the possible surface sites in a terrace-ledge-kink (TLK) model. (c) Dissolution energy barriers as a function of the dissolving site coordination. The value for dislocation sites (n = 4) is fixed, and linear relationships with different slopes are considered. (d) Dissolution rate for two cases: a covalent material (slope m) and an ionic material (slope 0.5 m). (e) Topology of the surfaces for a dissolving TLK surface with energy barriers defined according to different slopes gathered in Table 1. The color scale represents the depth of the surface. (For interpretation of the references to color in this figure legend, the reader is referred to the web version of this article.)

precipitation in this context refers to the backward dissolution reaction, and there is no precipitation of hydration products. The interplay between the dissolution and precipitation events give rise to a net dissolution rate that allowed us to reproduce the sigmoidal dissolution rate dependence with ΔG reported for most minerals [17]. However, the model is designed to work in undersaturated conditions and clearly C3S precipitation does not occur in such conditions.

The effective dissolution free energy ΔG^* can be related to its standard definition ΔG by looking at the equilibrium conditions when the dissolution and precipitation rates must be equal $r_d = r_p$. From Eqs. (3) and (4), and using a kink site ($n = 3$) as reference site for equilibrium [21], we can determine the equilibrium value of the effective ΔG^*:

$$\Delta G^* = RT \ln \frac{f_d}{f_p} + E_{p(n=3)} - E_{d(n=3)} \tag{6}$$

At the same time, according to the standard definition, ΔG is zero in equilibrium, so we obtain the relation between ΔG^* and ΔG:

$$\Delta G = \Delta G^* + RT \ln \frac{f_p}{f_d} + E_{d(n=3)} - E_{p(n=3)} \tag{7}$$

Hence, we can perform simulations at different effective dissolution free energies ΔG^*, and recalculate the corresponding dissolution free energy ΔG according to the dissolution and precipitation energies and frequencies.

2.2. Alite coarse grained model

C_3S is very hydrophilic and is known to pre-hydrate already at 63% relative humidity [22]. Recent ^{29}Si1H NMR data [23] indicates that the pre-hydrated surface includes hydroxide groups and partially hydroxylated silicate monomers without further polymerization. Molecular dynamics simulations agree with that finding [24,25], showing that in contact with water, the C_3S surface evolves quickly (in a few ns) into a partially hydrated amorphous interface. The disorder implies a large number of potential Ca coordination environments and reaction pathways, which makes it impossible to compute the precise dissolution and precipitation activation energies using atomistic simulations. Fortunately, the disorder at the atomic scale usually entails a homogenization of microscopic properties. Thus, we propose that disorder will translate into a homogenization of the energy barriers around 'mean values', and the specific energy barrier for a specific site will mainly depend on the coordination number rather than the crystallographic site.

We adopt the commonly used Kossel crystal or terrace-ledge-kink (TLK) model. The TLK model is a crystal with a cubic arrangement in which each lattice site has six neighbors with octahedral coordination in the bulk, which reduces to five-fold coordination in perfect surfaces, four in steps and dislocations, three in kink sites, and one in isolated atoms. In our case, each lattice site corresponds to a Ca_3SiO_5 structural unit, with a characteristic size of 4.85 Å calculated from the density of monoclinic and triclinic C_3S, see Fig. 2 [26,27]. Following the literature [28], we model edge dislocations by removing a single row of sites perpendicular to the surface. This method has been shown to reproduce qualitatively similar dissolution patterns as more detailed dislocation descriptions, including field stress and strain [28]. Also, for materials with low dissolution energy barriers, like C_3S, the edge, and screw dislocations have been proved to result in similar etch pit morphologies [28]. Therefore, pre-opened dissolution cores are enough to give a good description of the dislocation effect in our model.

2.3. Simulation details

All the KMC simulations are done using the KIMERA code [29]. KIMERA is an open-source code to study mineral dissolution with an efficient implementation of the reversible KMC model described in Section 2.1. It can model the dissolution of any system with atomic resolution [30] or use more general coarse-grained structures as we do in the present work. The dissolution events can be defined as 'site-by-site' or 'bond-by-bond'. The systems can be periodic in 1, 2, or 3 dimensions or isolated particles and can model different surface topographies, including dislocations, point defects, etc. [29]. KIMERA has a very flexible definition of dissolution reactions (or events) that can consider only first or second and higher order neighbors and additional structural conditions defined by the user. Despite KIMERA allowing multi-core simulations, we choose to run single-core simulations for this work since it offers better performance when a high number of them are done [29]. We will indicate below the specific details of the simulations for each section.

3. Results and discussion

3.1. Choice of model parameters

First, we need to define the parameters that govern dissolution, *i.e.,* dissolution activation energies $E_{di}(n)$ and f_d in Eq. (3). In covalent minerals like quartz, the activation energy $E_d(n)$ corresponds to the hydrolysis of a siloxane bond, and detailed values can be obtained from *ab-initio* simulations [30,31]. For C_3S, C_2S and CaO, the dissociation of water is spontaneous in several surface sites [24,25,32,33], so that is not the limiting process for dissolution. Other possibilities are cooperative surface topochemical reactions [32], desorption of mineral moieties from the surface [34–36], or proton-metal exchange reactions [37,38], including in the last the diffusion of protons that leave free spots for secondary water reactions [24,25]. Atomistic simulation can help identify those mechanisms, but quantifying the associated energy barriers is difficult, and the available data for C_3S is incomplete [35,39]. Therefore, we have used the macroscopic experimental values of the C_3S activation energy to infer the microscopic energy barriers. Thomas obtained activation energy for C_3S dissolution of 51.1 ± 1.8 kJ mol^{-1} [40], which remains constant over the first days of hydration. Juilland and Galluci performed experiments in isolated C_3S and obtained different activation energies depending on the undersaturation degree and the hydrodynamic conditions [18]. Close to equilibrium, the activation energy was ≈49 kJ mol^{-1}, very similar to the value obtained by Thomas, but it decreased down to ≈19 kJ mol^{-1} at very far from equilibrium conditions due to the change of limiting reaction from surface detachment to material transport [18]. Nicoleau et al. also made an estimation of E_a of 31 and 40 kJ mol^{-1} for different triclinic polymorphs based on the undersaturation at the onset of the etch pits opening [41]. As we discussed in our previous work [17], it is known that the activation energy for a mineral in the reaction-controlled regime roughly lays down between the energy barrier value of an atom placed close to a dislocation (or ledge atom) and of a kink atom. A higher amount of topological irregularities or a smaller grain size implies a higher density of kink atoms, and the macroscopic activation energy is shifted to the dissolution energy barrier for a kink atom. Conversely, the bigger the grain and the lower the number of defects and dislocations in its surface, the macroscopic activation energy is shifted to the dissolution energy barrier of the ledge/dislocation atoms. As starting point, we have attributed the experimental activation energy $E_a = 51$ kJ mol^{-1} to the dissolution energy barrier at ledge/dislocation $E_d(n = 4)$.

We have assigned the experimental activation energy from Thomas $E_d(n) = 51$ kJ mol^{-1} to the dissolution energy barrier for an atom close to a dislocation ($n = 4$). To determine the activation energy for the sites with other coordinations, it is common to use a linear function of the energy barrier proportional to the number of neighbors n. Such a relationship has been traditionally used for covalent materials. In contrast, C_3S possesses a marked ionic character, and the interface with water is expected to have a relatively homogeneous amorphous structure. According to those characteristics, the energy barriers for the different coordinations should be more homogeneous than in a covalent crystal, with closer values. To explore this effect, we have tested the dissolution rate far from equilibrium for four different linear relationships. We have set the energy for a 4 coordinated site and considered equidistant energies with different slopes m, 0.75 m, 0.5 m, and 0.25 m, see Table 1. We perform the simulations in a 200 × 200 × 100 Kossel crystal with periodic boundary conditions (PBC) along the surface. We place a single dislocation in the center of 1 × 1 cell wide and 100 cells deep, which corresponds to a dislocation density $d = 10^{10}$ cm^{-2} and lies in the known values reported for most minerals ($10^6 - 10^{10}$ cm^{-2}) [42].

Table 1
Dissolution energies for the studied energy relationships. All values in kJ mol^{-1}. Six coordinated bulk atoms are not reactive.

Site	Slope			
coord.	m	0.75 m	0.5 m	0.25 m
1	12.8	22.3	31.9	41.4
2	25.5	31.9	38.3	44.6
3	38.3	41.4	44.6	47.8
4	51.0	51.0	51.0	51.0
5	63.8	60.6	57.4	54.2

We observe important changes in the dissolution patterns depending on the relative differences of $E_d(n)$; see Fig. 2. In all cases, we observe the spontaneous nucleation of etch pits on the surface (mechanism III) and growth of the pre-opened dislocation (mechanism II), yet their relative contributions and step retreat patterns are different. For the largest differences between $E_d(n)$ (slope m, covalent material), the system tends to dissolve in stepwaves emanating from the etch pit, forming a 'train' of steps with large terraces (Fig. 2e). The dissolution rate, displayed in Fig. 2d, reaches a steady state nearly immediately with oscillations due to the variable perimeter of the dissolving steps. For the opposite case, with the smallest energy differences (slope 0.25 m, ionic material), the dissolution rate also reaches a steady state, with fewer oscillations. In this case, etch pits nucleate and grow very fast, at a rate comparable to the dislocation opening, due to their similar energy barriers (Fig. 2e). Therefore, the dislocation is not a preferential dissolution site, and the surface dissolves uniformly.

In the intermediate cases (slopes 0.75 m and 0.5 m), the predominant mechanism is also the dislocation opening in stepwaves, yet consecutive steps are closer, without large terraces between them. The etch pits are deep in their center, forming inverted pyramidal pits. This is more marked for the system with close energies (slope 0.5 m). These simulations display an acceleration of the dissolution rate with time. As the etch pit opens, the number of low coordinated sites at steps and kinks increases. The reactive area S_r increases, and consequently, the rate accelerates. It is interesting to note that the steady dissolution rate is very similar for the different energy sets and, therefore, independent of the dissolution mechanism. Overall, in view of the different etch pit morphology, dissolution mechanisms, and dissolution rate evolution, we have chosen the energy set with a slope of 0.5 m for our simulations. As we will see subsequently, it presents prominent mechanism II, as well as the formation of deep etch pits even at close to equilibrium conditions as it has been reported experimentally [2,18].

Once we have chosen a set of activation energies $E_d(n)$, we should define the fundamental dissolution frequency f_d. For that, we find the value that fits the experimental dissolution rate from [18] at far from equilibrium conditions (see Fig. 3). In those conditions, the ΔG^* in Eq. (4) is large and negative, and the exponential relationship makes precipitation negligible. Therefore, only dissolution, defined by Eq. (3), plays a role, and we can obtain the f_d value to fit the experiments. The obtained value to match the experiment is $f_d = 2.58 \cdot 10^9$ s^{-1}.

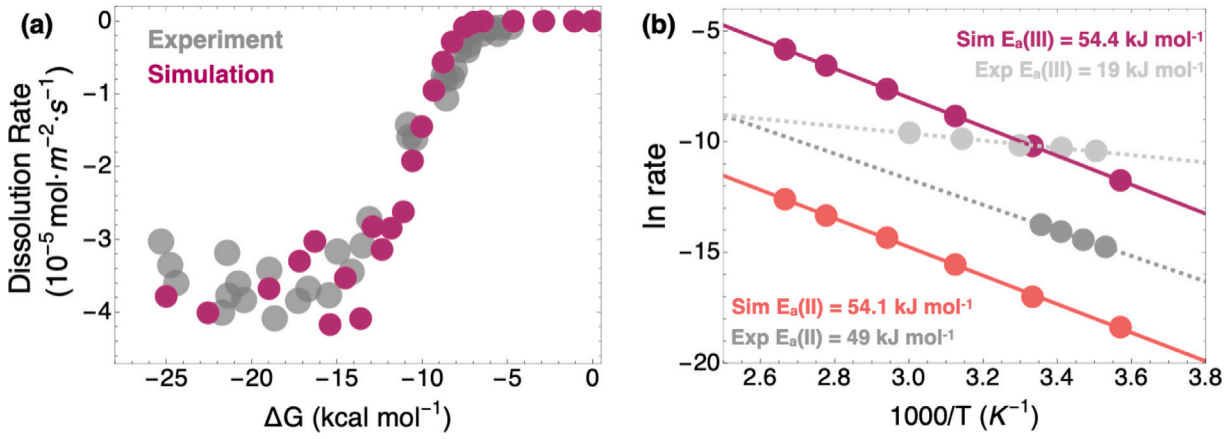

Fig. 3. (a) Alite dissolution rate with ΔG and its comparison with experimental data [18]. (b) Natural logarithm of the dissolution rate versus the inverse of temperature (Arrhenius plot). The activation energy is obtained from the linear regression. Change of activation energy in experiments [18] suggests a change of mechanism from surface controlled dissolution to transport controlled process.

The next step is to determine the precipitation parameters $E_p(n)$ and f_p in Eq. (4). Following the literature [43], we assume that the fundamental precipitation frequency f_p is equal to its dissolution counterpart. This is not necessarily true in all cases, especially for rigid materials like quartz [30], but it should be a good approach for flexible ionic materials like alite. The remaining parameter is the precipitation activation energy $E_p(n)$.

The kinetic parameters used in our model can be related to thermodynamic quantities in the standard state, *i.e.* far from equilibrium. In those conditions, the following relationships can be derived [44]:

$$\frac{f_d}{f_p}\exp\left(\frac{-E_d+E_p}{RT}\right)=\exp\left(\frac{T\Delta S^\circ-\Delta H^\circ}{RT}\right) \tag{8}$$

and therefore, the standard reaction enthalpy and entropy are directly related to the kinetic parameters:

$$\Delta H^\circ = E_d - E_p \tag{9}$$

$$\Delta S^\circ = R\ln\frac{f_d}{f_p} \tag{10}$$

The experimental enthalpy $\Delta H = -125$ [45], -128 [46] kJ mol^{-1} so the $E_p(n=3) = 188$ kJ mol^{-1}. We can infer $E_p(n=4)$ from the experimental $\Delta G_{crit.}$, where there is an onset in the dissolution rate due to mechanism change between I and II. From our previous work [17,47], we know that $\Delta G_{crit.}$ is related to $E_p(n=3)$ and $E_p(n=4)$ by the following equation in k_BT units:

$$\Delta G_{crit.} \approx \alpha + \left(E_{d(n=3)} - E_{d(n=4)} - E_{p(n=3)} + E_{p(n=4)}\right) + \ln\left(\frac{f_D}{f_p}\right) \tag{11}$$

where $\alpha = -2.3 \pm 0.9\ k_BT$ is a parameter that emerges by considering the center of the onset. For further information, refer to [47]. From this equation, we obtain that $E_p(n=4) = 151$ kJ mol^{-1}. The energy values for the rest of $E_p(n)$ are considered to follow a linear dependence with the previous two $E_p(n=3)$ and $E_p(n=4)$.

3.2. Activation energy and dissolution rate with ΔG

Using the parameters listed in Table 2, we have checked the ability of our model to reproduce the experimental data. For that, we use periodic surfaces with 100 × 100 sites in the surface direction, equivalent to 0.495 × 0.495 μm, and 50 sites of depth. We place a dislocation in the center of the system of 1 × 1 site width and 50 sites depth. This corresponds to a dislocation density of $4 \cdot 10^{10}$ cm^{-2}.

In Fig. 3a, we can see that our KMC results are in very good agreement with the dissolution experiments reported in [18]. The sigmoidal trend of the dissolution rate with ΔG is perfectly reproduced, as well as the critical free energy value $\Delta G_{crit.}$, when the transition between the low and high rates takes place. The transition regime, with mechanism II, is also well defined as in experiments [2], and the rate at far from equilibrium conditions is quite dispersed. The change between mechanism II and mechanism III is produced at $\Delta G = -20.3$ kcal mol^{-1}.

Table 2
Model parameters.

Parameter	Value
E_d(n) (kJ mol^{-1})	41.4, 44.6, 47.8, 51.0, 54.2
E_p(n) (kJ mol^{-1})	261.9, 224.5, 187.6, 151.0, 112.2
f_d (s^{-1})	$2.58 \cdot 10^9$
f_p (s^{-1})	$2.58 \cdot 10^9$

In Fig. 3b, we have calculated the macroscopic activation energy by doing simulations at different temperatures and fitting the results to the logarithmic form of the Arrhenius equation:

$$\ln r = \ln f_f - \frac{E_a}{R\cdot T} \tag{12}$$

We have done this fitting for two different values of ΔG to obtain the activation energies for mechanism II (simulation at $\Delta G = -9.5$ kcal mol^{-1}) and III (simulation at $\Delta G = -25$ kcal mol^{-1}). In the mechanism II regime, the obtained activation energy is $E_a(II) = 54.1 \pm 1.0$ kJ mol^{-1} in very good agreement with the experimental values from Juilland (49 kJ mol^{-1}) [18] and Thomas (51 kJ mol^{-1}) [40]. In the mechanism III regime, far from equilibrium, the obtained activation energy is $E_a(III) = 54.41 \pm 0.05$ kJ mol^{-1}. Interestingly, despite the switch from mechanism II to III, the activation energy does not change. The activation energy of each mechanism is independent of the fundamental frequency terms f_d and f_p, yet they change the dissolution rate. We can conclude that the limiting step in both cases is the same, the dislocation opening, and confirm that the experimental $E_a = 19$ kJ mol^{-1} at far from equilibrium conditions obtained by Juilland et al. implies a change of the dissolution limiting process from reaction controlled to diffusion controlled process [18]. This conclusion is also in agreement with the Molecular Dynamic simulation result of 11.5 kJ mol^{-1} for the diffusion energy barrier of Ca^{2+} ions on the surface [48].

As we used the experimental data to define our model parameters, it may seem a trivial task to reproduce it. However, the dissolution process has considerable complexity, involving nonlinear effects and transitions between different mechanisms. To the best of our knowledge, only the present KMC model and the one from Coopamootoo and Masoero [49] are able to replicate the dissolution rates as a function of the saturation index β.

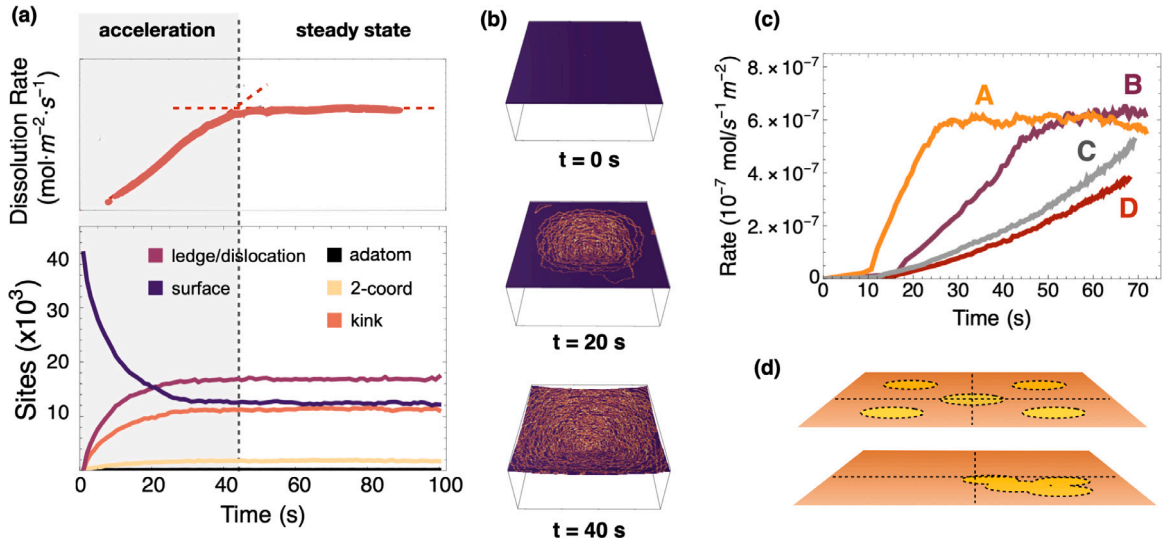

Fig. 4. (a) Time evolution of the dissolution rate (up) and quantity of atoms in different sites on the surface (down). The dotted line sets the steady state given by the coalescence of dislocations. (b) Snapshots at three different times. Initial configuration of a perfect surface with a dislocation in the center (t = 0 s), Beginning of the dislocation coalescence (t = 20 s), and steady state of the dissolution (t = 40 s). (c) Time evolution of the dissolution rate of different dislocation distributions gathered in Table 3. (d) Schematic representation of the initial dissolution of configuration (A) and (D) cases.

Table 3
Characteristics of the systems used to explore the acceleration period in Section 3.3.

sim.	Sites	Size (μm)	dis.	dens. (cm^{-2})	dist.
A	200	0.1 × 0.1	5	$5 \cdot 10^{10}$	homo
B	200	0.1 × 0.1	1	$1 \cdot 10^{10}$	homo
C	400	0.2 × 0.2	1	$2.5 \cdot 10^{9}$	homo
D	400	0.2 × 0.2	5	$1.25 \cdot 10^{10}$	hete

3.3. Acceleration period: dislocation opening

We turn now to analyze the acceleration of the dissolution rate. For that, we performed KMC simulations slightly above $\Delta G_{crit.}$, at $\Delta G = -10$ kcal mol^{-1} ($\beta = 0.98$) so that we can reproduce the experimental observations of alite dissolution in cement as close as possible: deep etch pitching and relative low dissolution rate because of close to equilibrium conditions [41]. At higher supersaturation, we observed a change from mechanism II to mechanism I, and a step-wave opening of the dislocations, inconsistent with experiments. At lower supersaturation, the dissolution rate is too high and incompatible with a realistic time scale.

First, we have done simulations in a system with 200 × 200 × 100 cells (0.1 μm × 0.1 μm and thickness 0.05 μm) with one dislocation in the center of the system, which correspond to a dislocation density of 10^{10} cm^{-2} (system B in Table 3). Fig. 4a shows the dissolution rate and the number of sites with different coordination as a function of time. As we can see, there is an acceleration of the dissolution rate with time until it reaches a maximum value, and then the system enters into a steady state regime. The rate evolution is correlated with the number of sites with a given coordination. Plain surfaces, *i.e.,* sites with coordination 5, at close to equilibrium conditions, do not dissolve appreciably, so the reactive area S_r can be ascribed to ledge and kink sites (3 and 4 coordination, respectively). As the dislocation opens and the etch pit grows, the number of reactive sites (ledge and kink sites) increases, and the nonreactive sites on the surface decrease. Hence, there is an increase in the reactive area and, consequently, the dissolution rate. When the etch pits merge (in this case, with itself through the PBCs), the number of sites with a given coordination becomes constant. S_r is maximum and constant over time, and the steady dissolution rate is reached.

The origin of the acceleration is clear and consistent with the mineral dissolution theory: an increase in the reactive area. To understand the effect of several properties on the magnitude of the acceleration, we have performed additional simulations for different dislocation densities and distributions, see Table 3. In general, it can be observed that the acceleration is faster in the systems with a higher dislocation density, A > B > C, and hence the steady state is reached in shorter times. It must be noted that the real parameter controlling the acceleration is the ratio between the reactive area and the total surface S_r/S_t. Take, for instance, systems B and C: they both have the same number of dislocations, so the etch pit opening and the number of reactive sites are the same, and so it is the steady state dissolution. However, in system C, with lower dislocation density, the acceleration is slower because the S_r/S_t ratio is smaller. This is a consequence of the dissolution rate units being normalized by the total area.

In systems A, B, and C, the distribution of dislocations is homogeneous; in other words, the distance between dislocations is the largest possible one. System D has five dislocations close to each other, and despite the dislocation density being the second highest, just after system A, its acceleration is the slowest. The dislocations merge soon after the dissolution starts, and the effective S_r/S_t ratio is equivalent to a system with a single dislocation. Therefore, besides the dislocation density, also the dislocation arrangement plays a crucial role in the (surface normalized) dissolution rate. Finally, we note that the steady-state rate is the same for any dislocation density, and its only effect is how fast it is reached, as proposed by Lasaga and Luttge [14,50].

3.4. Deceleration period: dislocation exhaustion

We move now to give a possible explanation for the deceleration period, the so-called dislocation exhaustion. As we have explained before, the dissolution rate reaches a steady state when the dissolution fronts from adjacent dislocation merge. The dissolution theory [2] proposed that such a dislocation coalescence should decrease the reactive area and, consequently, the dissolution rate. Nevertheless, our simulations indicate that the reactive area is maintained constant after coalescence, as explained before (4a). The acceleration corresponds to an increase in the reactive area, but no deceleration is observed upon coalescence.

According to our model and simulations, the only possible mechanism to reduce the reactive area and hence the reaction rate is dislocation exhaustion. It is known that in crystals, the number of

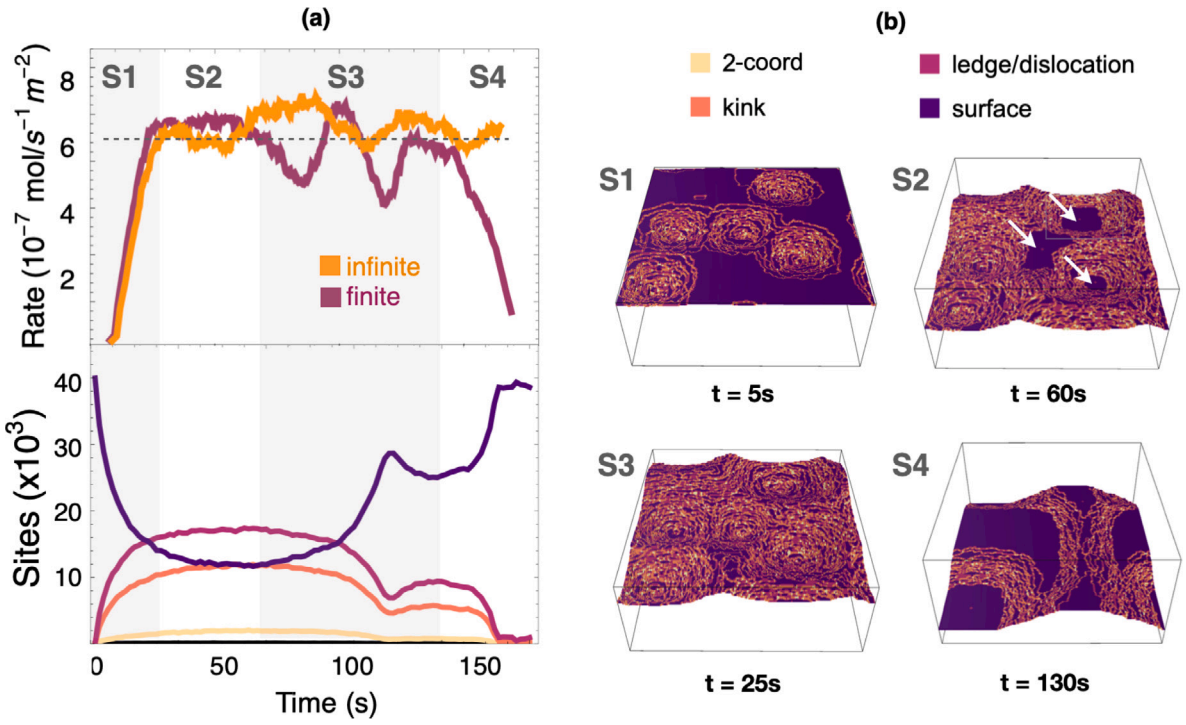

Fig. 5. (a) Time evolution of the dissolution rate (up) and site distribution (down) for a system with five dislocations of different finite depths. (b) Snapshots at the beginning of the coalescence (t = 5 s), steady state of the dissolution (t = 25 s), exhaustion of three of the dislocations (t = 60 s), and exhaustion of the last dislocation (t = 130 s). Sequential exhaustion of dislocations decreases the dissolution rate locally until the last of the dislocations is dissolved. (For interpretation of the references to color in this figure legend, the reader is referred to the web version of this article.)

dislocations decreases with depth. For $SrTiO_3$ oxide, for example, the dislocation density reduces from $6 \cdot 10^9$ cm^{-2} in the surface to $\sim 10^8$ cm^{-2} in a depth of 40 μm [51]. If that is also the case in alite, when the dissolution reaches the bottom of a dislocation site, we can expect a decrease in the reactive area and, consequently, a decrease in the dissolution rate.

To investigate dislocation exhaustion, we performed simulations in two systems of 200 × 200 sites, with five dislocations randomly distributed at the surface. In one case, the dislocations are of infinite length, and in the other, of finite length, with variable depths between 100 nm and 300 nm (between 20% and 60% of the system thickness). In Fig. 5a, we show the dissolution rate as a function of time for both systems and the number of sites with different coordination for the case of finite dislocations. The snapshots in Fig. 5b at 4 different times match the four stages (S1 to S4) in Fig. 5a, and the color scale indicates the site coordination.

Both systems display a similar acceleration (stage S1, time 5 s) while the etch pits grow and reach the same maximum rate when the dissolution fronts merge (stage S2, t = 25 s). After that, the dissolution reaches the bottom of a dislocation, and the exposed sites for dissolution are no longer undercoordinated ($n = 3, 4$) but perfect surface sites ($n = 5$), without a tendency to dissolve (stage S3, t = 60 s). This new nonreactive surface can be observed in the corresponding snapshots at t = 60 s indicated with a white arrow. As a consequence, the dissolution rate decreases, yet there is a new acceleration period when the growth of etch pits from deeper dislocations consumes the new nonreactive surface. As heterogeneous dislocation depths are used in the simulation, several deceleration and acceleration steps are observed. Finally, when all dislocations are consumed (stage S4, t = 130 s), there is a deceleration as the S_r decreases and the nonreactive area becomes dominant. Eventually, a steady rate should be reached corresponding to the new limiting process, that is, the spontaneous opening of a dissolution core in the surface.

Overall, we conclude that the coalescence of dislocations will not reduce the reactive area of the crystal under ideal conditions. One possible mechanism to reduce the dissolution rate is the exhaustion of dislocations.

4. Discussion

The present KMC model has proved useful for understanding the fundamental aspects of the C_3S dissolution mechanism. However, the KMC model has limitations that may play a role in determining the actual dissolution mechanism, which are worth discussing.

With the current model, we are able to show a clear distinction in the etch pit growth morphology as a function of the activation energy difference between coordination, which we attribute to a more ionic or covalent character. Then, assuming the ionic model for C_3S, we can observe acceleration and deceleration based on the etch pit opening and exhaustion, respectively. Although the evolution of the surface topology is a key aspect in interpreting dissolution process, we do not fully reproduce the etch pit morphology observed in C_3S micrographs [41], which are usually shallower than what we achieve in our simulations. Fortunately, the aspect ratio of the dislocation is not crucial for the proposed acceleration and deceleration mechanisms. If anything, shallower pits could further support the deceleration by dislocation exhaustion, as the lateral growth that governs dislocation coalescence would be slower than the deep growth relevant for dislocation exhaustion. Nevertheless, there are at least three key aspects not included in the model that could modify the simulation outcome and correct the etch pit aspect ratio.

First, etch pits with a shallow shape can be achieved if the actual atomic structure of a crystal is taken into account instead of using a coarse grained approach. Indeed, for belite, we have observed etch pits growing deeper than wider using KIMERA [52]. It is also interesting to note the connection between the surface amorphization and the dislocations. If the surface is distorted and loses its crystalline features, the forces induced by the dislocations, which makes them preferential dissolution sites, may decrease or even vanish. However, using an ordered atomic structure is hardly reconcilable with the idea of a disordered hydration layer due to fast hydration, as observed from

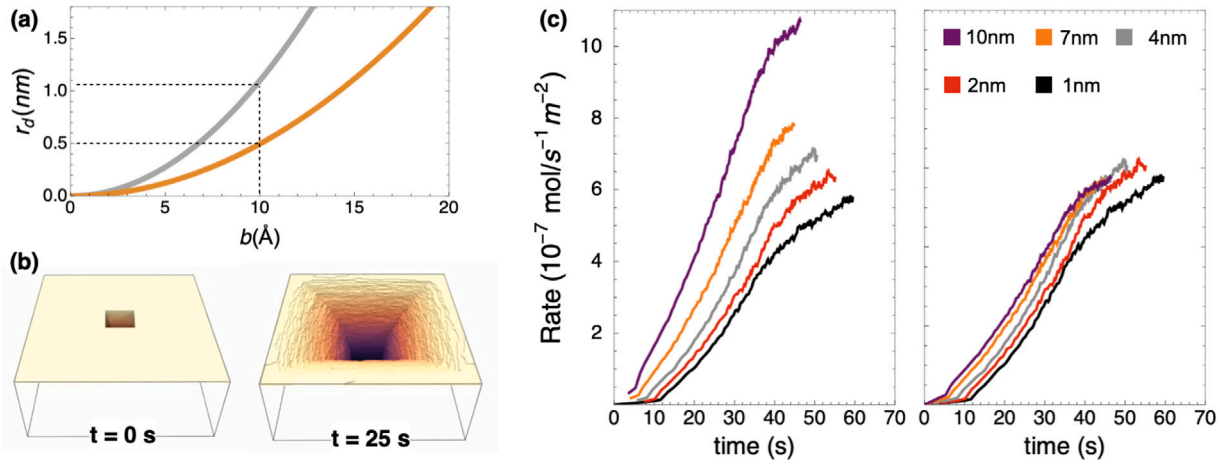

Fig. 6. (a) radius of a hollow core as a function of the burger's vector b for two limit cases. In gray, γ = 0.75 J/m and G = 65 GPa. In orange γ = 1.15 J/m and G = 55 GPa. (b) Snapshots of a simulation of a dissolving hollow core at t = 0 s and t = 25 s. (c) Dissolution rate as a function of time for dissolving hollow cores of different radius. The same plot but considering the surface of the hollow core walls to compute the dissolution rates. (For interpretation of the references to color in this figure legend, the reader is referred to the web version of this article.)

simulations and experiments [23,25,53]. Further MD simulations will be necessary to understand the real C_3S/water interface.

Second, we did not consider surface diffusion of adatoms, which has been shown to reproduce the formation of shallow topologies even with a Kossel crystal model [14,54,55]. The adatoms diffuse from surface sites to undercoordinated kinks in the opening etch pits, reducing undercoordination and delaying the lateral growth. However, we ignored this additional level of complexity due to the nature of the material. It is relatively easy to understand that surface diffusion may take place in certain materials like metals or salts. On the contrary, for oxides it is less intuitive, as the diffusion should entail a more complex rearrangement of the metal cation together with oxygen atoms to maintain electroneutrality. A more sophisticated model must be devised to reconcile the diffusion process with the iono-covalent bonding scheme in C_3S. For instance, the adsorption of small C-S-H complexes or prenucleation clusters (PNCs) as those reported in [56] could play a similar role as diffusion: the complexes could adsorb preferentially on the surface kinks, delaying etch pit lateral growth, and favoring deeper morphologies.

Third, we work under constant undersaturation conditions. That is not the case for real C_3S dissolution, yet controlled experiments can impose a constant ΔG. However, we think that it could be interesting to explore the role of *local* undersaturation. In a fast dissolving system the diffusion of ions in solution might be of the same order than the dissolution, and therefore the saturation close to the opening etch pits could be higher. The saturation value could also fluctuate due for instance to C-S-H precipitation among other physico-chemical mechanisms. These coupled processes depend on time and are hard to predict. Currently, the implementation of variable ΔG in time and space in KIMERA is in progress.

In addition to the three aspects discussed above, the presence of hollow cores could help better reproduce the observed topologies and explain some of the model disagreement. Hollow cores or micropipes are crystallographic defects that induce the formation of large holes from a dislocation, usually for crystals with large burgers vectors b [57], see Fig. 6. If hollow cores were present in C_3S, they would act as preferential dissolution sites like a regular dislocation, and the surface relaxation due to the amorphization would not compensate the low coordination. In addition, shallow morphologies would develop naturally from the hollow core. According to Frank's theory [57], the radius of a hollow core r_f depends of the following relationship:

$$r_f = \frac{Gb^2}{\gamma 8\pi^2} \tag{13}$$

where G is the shear modulus, γ the surface energy and b the Burger's vector. In Fig. 6 we show the hollow core radius in C_3S as a function of the burgers vector magnitude for two limit cases depending on the surface energies γ and shear moduli G values reported in the literature [24,58,59]. The gray line depicts an upper limit (with high shear modulus and low surface energy) and the orange line a lower limit (with low shear modulus and high surface energy). The burgers vector magnitude is usually of the order of the lattice dimension, yet materials with hollow cores have very large burgers vectors, like SiC [60] or $Ba(NO_3)_2$ [61]. For the typical unit cell dimension of ~10 Å [26,27], indicated with the dashed line in Fig. 6, the hollow core radius is between 1 and 2 of our lattice sites. With these values, micropipes should not form in C_3S, unless it has an anomalously large burgers vector. Nevertheless, we have tested the dissolution rate evolution as a function of time for a system with a hollow core of different radii, from 1 nm to 10 nm, see Fig. 6c. We found that the acceleration is faster for larger hollow cores as expected, because the number of undercoordinated sites is larger. Therefore, when we normalize the dissolution rate by the reactive area, *i.e.,* the undercoordinated surface that includes the area of the micropipe walls, we observe that the rate is equal (right panel in Fig. 6c). Thus, we can conclude that hollow cores do not change the dissolution mechanism, only the available reactive surface area.

5. Conclusions

In this work, we studied alite dissolution by Kinetic Monte Carlo (KMC) simulations. We built a Kossel crystal coarse-grained model to represent the alite-water disordered interface, and we fit the reaction energy barriers and frequencies based on experimental observations. Despite the simplicity of the model, the main features of C_3S dissolution were captured, including the formation of etch pits, the macroscopic activation energies, and the dissolution rate dependence with ΔG. Furthermore, important implications regarding the acceleration and deceleration of the dissolution rate were obtained.

The simulations were able to capture with precision the three dissolution mechanisms as a function of the Gibbs free energy ΔG. The macroscopic activation energies of C_3S dissolution are very similar along the different mechanisms: $E_{a,II}$ = 54.1 ± 1.0 kJ mol^{-1} and $E_{a,III}$ = 54.41 ± 0.05 kJ mol^{-1} kJ mol^{-1}. This value is in agreement with the experimental observation if no transportation effect is involved, 51.1 ± 1.8 kJ mol^{-1} [40] and E_a = 49 kJ mol^{-1} [18] and indicates that despite the dramatic increase of the dissolution rate from mechanism

II to III, more than one order of magnitude, its limiting factor remains the shame, the dislocation opening.

The acceleration of the hydration rate can be ascribed to the increase of reactive area as the etch pits open on the surface. This agrees with the dissolution theory interpretation of cement acceleration period [2,16]. According to our simulations, two conditions have to be met. First, the dissolution energies as a function of the coordination must be close in value (ionic material). Second, the dissolution must be at close to equilibrium conditions. However, the deceleration phase cannot be ascribed to the coalescence of dislocations as suggested in the dissolution theory [2,16]. It has been observed that dislocation coalescence entails reaching the maximum reactive surface and, consequently, the maximum dissolution rate, which remains constant. Still, within the mineral dissolution theory framework, we suggest dislocation exhaustion as a plausible explanation for the deceleration in C_3S dissolution. When the dissolution reaches the bottom of a dislocation site, the reactive area decreases, and so does the dissolution rate. The hypothetical presence of hollow cores would not change the proposed mechanism.

Overall, we show that mineral dissolution theory can explain the acceleration and deceleration of alite dissolution. Yet, we cannot rule out that the role of C-S-H nucleation and growth can be more important in the deceleration stage. In fact, we have to assume dislocation exhaustion which has not been reported in experiments. Further work will be needed to understand the dissolution rate evolution, including extensions of our KMC code to take into account the time evolution and local fluctuations of the saturation index at different surface regions, especially close to the dissolving etch pits.

CRediT authorship contribution statement

Pablo Martin: Conceptualization, Formal analysis, Investigation, Methodology, Software, Validation, Writing – original draft, Writing – review & editing. **Juan J. Gaitero:** Conceptualization, Supervision, Validation, Writing – review & editing. **Xabier M. Aretxabaleta:** Investigation, Validation, Writing – review & editing. **Mohammad Javad Abdolhosseini Qomi:** Formal analysis, Funding acquisition, Investigation, Supervision, Validation, Writing – review & editing. **Hegoi Manzano:** Conceptualization, Data curation, Funding acquisition, Investigation, Supervision, Validation, Writing – original draft, Writing – review & editing.

Declaration of competing interest

The authors declare the following financial interests/personal relationships which may be considered as potential competing interests: Hegoi Manzano reports financial support was provided by Government of the Basque Country Department of Education Linguistic Policy and Culture. Pablo Martin reports financial support was provided by Government of Spain Ministry of Universities. M.J.A Qomi reports financial support was provided by National Science Foundation.

Data availability

Data will be made available on request.

Acknowledgments

The authors would like to acknowledge funding from ‘Departamento de Educación, Política Lingüística y Cultura del Gobierno Vasco’ (Grant No. IT1458-22), the Transnational Common Laboratory ‘Aquitaine-Euskadi Network in Green Concrete and Cement-based Materials’ (LTC-Green Concrete) and the technical and human support provided by the Scientific Computing Service of SGIker (UPV/EHU/ERDF, EU). P.M. also acknowledges the postdoctoral fellowship ‘Margaritas Salas scholarship NEXT GENERATION EU.’ from ‘ministerio de universidades de España’. MJAQ acknowledges funding from the United States’ National Science Foundation under awards CMMI-2145537 and CMMI-2103125.

References

[1] K. Scrivener, A. Ouzia, P. Juilland, A.K. Mohamed, Advances in understanding cement hydration mechanisms, Cem. Concr. Res. 124 (2019) 105823.

[2] P. Juilland, L. Nicoleau, R.S. Arvidson, E. Gallucci, Advances in dissolution understanding and their implications for cement hydration, RILEM Tech. Lett. 2 (2017) 90–98, http://dx.doi.org/10.21809/rilemtechlett.2017.47, URL: http://letters.rilem.net/index.php/rilem/article/view/47.

[3] E. John, B. Lothenbach, Cement hydration mechanisms through time–a review, J. Mater. Sci. (2023) 1–29.

[4] J.W. Bullard, H.M. Jennings, R.A. Livingston, A. Nonat, G.W. Scherer, J.S. Schweitzer, K.L. Scrivener, J.J. Thomas, Mechanisms of cement hydration, Cem. Concr. Res. 41 (12) (2011) 1208–1223.

[5] K.L. Scrivener, A. Nonat, Hydration of cementitious materials, present and future, Cem. Concr. Res. 41 (7) (2011) 651–665, http://dx.doi.org/10.1016/j.cemconres.2011.03.026, URL: http://www.sciencedirect.com/science/article/pii/S0008884611001025. Special Issue: 13th International Congress on the Chemistry of Cement.

[6] K.L. Scrivener, P. Juilland, P.J. Monteiro, Advances in understanding hydration of Portland cement, Cem. Concr. Res. 78 (2015) 38–56, http://dx.doi.org/10.1016/j.cemconres.2015.05.025, URL: http://www.sciencedirect.com/science/article/pii/S0008884615001623. Keynote papers from 14th International Congress on the Chemistry of Cement (ICCC 2015).

[7] J.J. Thomas, J.J. Biernacki, J.W. Bullard, S. Bishnoi, J.S. Dolado, G.W. Scherer, A. Luttge, Modeling and simulation of cement hydration kinetics and microstructure development, Cem. Concr. Res. 41 (12) (2011) 1257–1278.

[8] M. Avrami, Kinetics of phase change. I general theory, J. Chem. Phys. 7 (12) (1939) 1103–1112.

[9] J.J. Thomas, A new approach to modeling the nucleation and growth kinetics of tricalcium silicate hydration, J. Am. Ceram. Soc. 90 (10) (2007) 3282–3288.

[10] S. Bishnoi, K.L. Scrivener, Studying nucleation and growth kinetics of alite hydration using μic, Cem. Concr. Res. 39 (10) (2009) 849–860, http://dx.doi.org/10.1016/j.cemconres.2009.07.004, URL: https://www.sciencedirect.com/science/article/pii/S0008884609001641.

[11] G.W. Scherer, J. Zhang, J.J. Thomas, Nucleation and growth models for hydration of cement, Cem. Concr. Res. 42 (7) (2012) 982–993, http://dx.doi.org/10.1016/j.cemconres.2012.03.019, URL: https://www.sciencedirect.com/science/article/pii/S0008884612000725.

[12] A. Ouzia, K. Scrivener, The needle model: a new model for the main hydration peak of alite, Cem. Concr. Res. 115 (2019) 339–360.

[13] E. Masoero, J.J. Thomas, H.M. Jennings, A reaction zone hypothesis for the effects of particle size and water-to-cement ratio on the early hydration kinetics of C3S, J. Am. Ceram. Soc. 97 (3) (2014) 967–975.

[14] A.C. Lasaga, A. Luttge, Variation of crystal dissolution rate based on a dissolution stepwave model, Science 291 (5512) (2001) 2400–2404, http://dx.doi.org/10.1126/science.1058173, URL: https://science.sciencemag.org/content/291/5512/2400. arXiv:https://science.sciencemag.org/content/291/5512/2400.full.pdf.

[15] P.M. Dove, N. Han, J.J. De Yoreo, Mechanisms of classical crystal growth theory explain quartz and silicate dissolution behavior, Proc. Natl. Acad. Sci. 102 (43) (2005) 15357–15362, http://dx.doi.org/10.1073/pnas.0507777102, URL: https://www.pnas.org/content/102/43/15357. arXiv:https://www.pnas.org/content/102/43/15357.full.pdf.

[16] P. Juilland, E. Gallucci, R. Flatt, K. Scrivener, Dissolution theory applied to the induction period in alite hydration, Cem. Concr. Res. 40 (6) (2010) 831–844.

[17] P. Martin, H. Manzano, J.S. Dolado, Mechanisms and dynamics of mineral dissolution: A new kinetic Monte Carlo model, Adv. Theory Simul. 2 (10) (2019) 1900114.

[18] P. Juilland, E. Gallucci, Morpho-topological investigation of the mechanisms and kinetic regimes of alite dissolution, Cem. Concr. Res. 76 (2015) 180–191.

[19] V. Robin, B. Wild, D. Daval, M. Pollet-Villard, A. Nonat, L. Nicoleau, Experimental study and numerical simulation of the dissolution anisotropy of tricalcium silicate, Chem. Geol. 497 (2018) 64–73, http://dx.doi.org/10.1016/j.chemgeo.2018.08.023, URL: http://www.sciencedirect.com/science/article/pii/S0009254118304200.

[20] L. Nicoleau, M.A. Bertolim, Analytical model for the alite (C3S) dissolution topography, J. Am. Ceram. Soc. 99 (3) (2016) 773–786, http://dx.doi.org/10.1111/jace.13647, arXiv:https://ceramics.onlinelibrary.wiley.com/doi/pdf/10.1111/jace.13647. URL: https://ceramics.onlinelibrary.wiley.com/doi/abs/10.1111/jace.13647.

[21] A.C. Lasaga, A. Luttge, Mineralogical approaches to fundamental crystal dissolution kinetics, Amer. Mineral. 89 (4) (2004) 527–540, http://dx.doi.org/10.2138/am-2004-0407, arXiv:https://pubs.geoscienceworld.org/msa/ammin/article-pdf/89/4/527/3618798/07_8751Luttge_layout.pdf. URL: https://doi.org/10.2138/am-2004-0407.

[22] M. Whittaker, E. Dubina, F. Al-Mutawa, L. Arkless, J. Plank, L. Black, The effect of prehydration on the engineering properties of CEM I Portland cement, Adv. Cem. Res. 25 (1) (2013) 12–20, http://dx.doi.org/10.1680/adcr.12.00030, arXiv:https://doi.org/10.1680/adcr.12.00030.

[23] E. Pustovgar, R.P. Sangodkar, A.S. Andreev, M. Palacios, B.F. Chmelka, R.J. Flatt, J.-B.d. de Lacaillerie, Understanding silicate hydration from quantitative analyses of hydrating tricalcium silicates, Nat. Commun. 7 (1) (2016) 1–9.
[24] H. Manzano, E. Durgun, I. López-Arbeloa, J.C. Grossman, Insight on tricalcium silicate hydration and dissolution mechanism from molecular simulations, ACS Appl. Mater. Interfaces 7 (27) (2015) 14726–14733.
[25] C. Qi, H. Manzano, D. Spagnoli, Q. Chen, A. Fourie, Initial hydration process of calcium silicates in Portland cement: a comprehensive comparison from molecular dynamics simulations, Cem. Concr. Res. 149 (2021) 106576.
[26] F. Dunstetter, M.-N. De Noirfontaine, M. Courtial, Polymorphism of tricalcium silicate, the major compound of Portland cement clinker: 1. Structural data: review and unified analysis, Cem. Concr. Res. 36 (1) (2006) 39–53.
[27] F. Nishi, Y. Takeuchi, I. Maki, Tricalcium silicate ca30 (SiO4): The monoclinic superstructure, Z. Kristallogr. 172 (1985) 297–314.
[28] P. Meakin, K.M. Rosso, Simple kinetic Monte Carlo models for dissolution pitting induced by crystal defects, J. Chem. Phys. 129 (20) (2008) 204106.
[29] P. Martin, J.J. Gaitero, J.S. Dolado, H. Manzano, KIMERA: A kinetic Montecarlo code for mineral dissolution, Minerals 10 (9) (2020) 825.
[30] P. Martin, J.J. Gaitero, J.S. Dolado, H. Manzano, New kinetic Monte Carlo model to study the dissolution of quartz, ACS Earth Space Chem. 5 (3) (2021) 516–524.
[31] A. Pelmenschikov, J. Leszczynski, L.G. Pettersson, Mechanism of dissolution of neutral silica surfaces: Including effect of self-healing, J. Phys. Chem. A 105 (41) (2001) 9528–9532.
[32] H. Manzano, R.J. Pellenq, F.-J. Ulm, M.J. Buehler, A.C. van Duin, Hydration of calcium oxide surface predicted by reactive force field molecular dynamics, Langmuir 28 (9) (2012) 4187–4197.
[33] Q. Wang, H. Manzano, Y. Guo, I. Lopez-Arbeloa, X. Shen, Hydration mechanism of reactive and passive dicalcium silicate polymorphs from molecular simulations, J. Phys. Chem. C 119 (34) (2015) 19869–19875.
[34] A.G. Stack, P. Raiteri, J.D. Gale, Accurate rates of the complex mechanisms for growth and dissolution of minerals using a combination of rare-event theories, J. Am. Chem. Soc. 134 (1) (2012) 11–14.
[35] Y. Li, H. Pan, Q. Liu, X. Ming, Z. Li, Ab initio mechanism revealing for tricalcium silicate dissolution, Nature Commun. 13 (1) (2022) 1253.
[36] Y. Tao, S. Zare, F. Wang, M.J.A. Qomi, Atomistic thermodynamics and kinetics of dicalcium silicate dissolution, Cem. Concr. Res. 157 (2022) 106833.
[37] W.H. Casey, C. Ludwig, The mechanism of dissolution of oxide minerals, Nature 381 (6582) (1996) 506–509.
[38] S. Zare, A. Funk, M.J. Abdolhosseini Qomi, Formation and dissolution of surface metal carbonate complexes: Implications for interfacial carbon mineralization in metal silicates, J. Phys. Chem. C 126 (28) (2022) 11574–11584.
[39] K. Salah Uddin, B. Middendorf, Reactivity of different crystalline surfaces of C3S during early hydration by the atomistic approach, Materials 12 (9) (2019) 1514, http://dx.doi.org/10.3390/ma12091514.
[40] J.J. Thomas, The instantaneous apparent activation energy of cement hydration measured using a novel calorimetry-based method, J. Am. Ceram. Soc. 95 (10) (2012) 3291–3296.
[41] L. Nicoleau, A. Nonat, D. Perrey, The di- and tricalcium silicate dissolutions, Cem. Concr. Res. 47 (2013) 14–30, http://dx.doi.org/10.1016/j.cemconres.2013.01.017, URL: http://www.sciencedirect.com/science/article/pii/S0008884613000240.
[42] H.H. Teng, Controls by saturation state on etch pit formation during calcite dissolution, Geochim. Cosmochim. Acta 68 (2) (2004) 253–262.
[43] A.C. Lasaga, A.C. Lasaga, Kinetic Theory in the Earth Sciences, vol. 811, JSTOR, 1998.
[44] S.L. Brantley, J.D. Kubicki, A.F. White, Kinetics of Water-Rock Interaction, vol. 168, Springer, 2008.
[45] S. Bergold, F. Goetz-Neunhoeffer, J. Neubauer, Mechanically activated alite: New insights into alite hydration, Cem. Concr. Res. 76 (2015) 202–211.
[46] F. Bellmann, T. Sowoidnich, B. Möser, Formation of an intermediate phase and influence of crystallographic defects on dissolution of C3S, in: Proceedings of 13th ICCC, Instituto de Ciencias de la Construccion “eduardo Torroja”, Madrid, Spain, 2011.
[47] P. Martín García, Study of mineral dissolution by kinetic Monte Carlo simulations, 2020.
[48] Y. Tao, S. Zare, F. Wang, M.J.A. Qomi, Atomistic thermodynamics and kinetics of dicalcium silicate dissolution, Cem. Concr. Res. 157 (2022) 106833.
[49] K. Coopamootoo, E. Masoero, Simulations of crystal dissolution using interacting particles: prediction of stress evolution and rates at defects and application to tricalcium silicate, J. Phys. Chem. C 124 (36) (2020) 19603–19615.
[50] A.C. Lasaga, A. LUTTGE, A model for crystal dissolution, Eur. J. Mineral. 15 (4) (2003) 603–615.
[51] K. Szot, C. Rodenbücher, G. Bihlmayer, W. Speier, R. Ishikawa, N. Shibata, Y. Ikuhara, Influence of dislocations in transition metal oxides on selected physical and chemical properties, Crystals 8 (6) (2018) 241.
[52] Mesoscopic mechanisms of dicalcium silicate, 2023, URL: https://papers.ssrn.com/sol3/papers.cfm?abstract_id=4570976.
[53] D. Marchon, R. Flatt, Impact of chemical admixtures on cement hydration, 2016, pp. 279–304.
[54] A. Lüttge, R.S. Arvidson, C. Fischer, A stochastic treatment of crystal dissolution kinetics, Elements 9 (3) (2013) 183–188.
[55] A.C. Lasaga, A.E. Blum, Surface chemistry, etch pits and mineral-water reactions, Geochim. Cosmochim. Acta 50 (10) (1986) 2363–2379.
[56] X.M. Aretxabaleta, J. López-Zorrilla, I. Etxebarria, H. Manzano, Multi-step nucleation pathway of CSH during cement hydration from atomistic simulations, Nature Commun. 14 (1) (2023) 7979.
[57] F. Frank, Capillary equilibria of dislocated crystals, Acta Crystallogr. 4 (6) (1951) 497–501.
[58] J. Claverie, Q. Wang, S. Kamali-Bernard, F. Bernard, Assessment of the reactivity and hydration of Portland cement clinker phases from atomistic simulation: A critical review, Cem. Concr. Res. 154 (2022) 106711.
[59] H. Manzano, J. Dolado, A. Ayuela, Elastic properties of the main species present in Portland cement pastes, Acta Mater. 57 (5) (2009) 1666–1674.
[60] H. Matsuhata, H. Yamaguchi, T. Ohno, Analysis of contrasts and identifications of Burgers vectors for basal-plane dislocations and threading edge dislocations in 4H-SiC crystals observed by monochromatic synchrotron X-ray topography in grazing-incidence Bragg-case geometry, Phil. Mag. 92 (36) (2012) 4599–4617.
[61] M. Plomp, K. Maiwa, W. van Enckevort, Atomic force microscopy observations of hollow cores on the {1 1 1} and {1 0 0} faces of barium nitrate, J. Cryst. Growth 198 (1999) 246–252.